Electronic Supplementary Material (ESI) for EES Catalysis.

Epitaxially Heterointerficial Electron Bridge Synchoronizes Oxygen Evolution Activity and Stability on a Layered Double Hydroxide Surface

Jia Wang,[ab] Zelin Zhao,[b] Min Guo,[c] Liang Xiao,[b] Haolin Tang,[de] Jiantao Li,*[a] Zongkui Kou *[d] and Junsheng Li *[be]

[a.] *School of Materials Science and Engineering, Wuhan University of Technology, Wuhan 430070, P. R. China.*
[b.] *School of Chemistry, Chemical Engineering and Life Sciences, Wuhan University of Technology, Wuhan 430070, P. R. China.*
[c.] *School of Mechanical and Electronic Engineering, Wuhan University of Technology, Wuhan 430070, P. R. China.*
[d.] *State Key Laboratory of Advanced Technology for Materials Synthesis and Processing, Wuhan 430070, P. R. China.*
[e.] Foshan Xianhu Laboratory of the Advanced Energy Science and Technology Guangdong Laboratory, Foshan 528200, P. R. China.
*Corresponding authors: Jiantao Li (Jiantao.li@anl.gov), Zongkui Kou (zongkuikou@whut.edu.cn), Junsheng Li (li_j@whut.edu.cn)

Experimental Section

Materials

Ferric nitrate nonahydrate (Innochem AR), cobalt nitrate hexahydrate (Aladdin AR 99%), urea (Aladdin AR), ethanol (Sinopharm AR), potassium hydroxide (Sinopharm AR), high-purity argon (Xiangyun 99.999%). All chemicals were used without further purification. Nickel (Innochem 0.98m × 1m × 1mm, 99.99%).

Catalyst Preparation

The LDH*/NFO with the electron bridge of $Ni(OH)_2$ was elaborately equipped through a two-step method. Prior to synthesis, a piece of NF (1 × 2 cm^2) was cleaned with 3 M HCl, acetone, ethanol and deionized water for 10 min in turn with the participation of ultrasound. After drying at 30 ℃ for 2 hs under vacuum, the deep-cleaned NF was collected for introducing buffer layers. Briefly, the NF was subjected to CVs at the range of 1.2 V - 1.6 V (vs. RHE) and galvanostatic polarization for 10 min at 20 mA uninterrupted in 1 M KOH. After rinsing thoroughly with deionized water for residue removal, the NF was transferred to 60 mL deionized water including 0.25 mmol $Fe(NO_3)_3$ $9H_2O$ and stirred for 10 minutes. Then, 0.75 mmol $Co(NO_3)_2$ $9H_2O$ and 2 mmol urea were dissolved in the above solution, respectively. After stirring for 30 min, the mixture was transferred into a 100 mL Teflon-lined steel vessel and maintained at 120 ℃ for 10 hs. After cooling to room temperature, the NF was rinsed with deionized water and ethanol 3 times, respectively and then dried in a vacuum at 60 ℃ for 2 hs. For comparison, the FeCo-LDH supported on NF without the buffer layers of $Ni(OH)_2$ (denoted as LDH/NF) and the innocent FeCo-LDH (denoted as FC) were prepared also through the equal method except without the process of electrochemical oxidation for NF and absence of NF, respectively. Given the imprecise quantification for active component (FeCo-LDH), the loading is acquired as 0.512 mg cm^{-2} via recording the quality change of NF before and after the hydrothermal process in 3 repetition experiments. For accuracy in performance evaluated, the electrodes of RuO_2 and pristine FC were equipped with the loading of 0.512 mg/cm^2 on NF.

Materials characterization

Field emission transmission electron microscopy (TEM) and **high-resolution TEM** (HRTEM) studies were performed using a FEI Talos F200x transmission electron microscope operated at 200 kV.

High-angle aberration-corrected dark-field scan transmission electron microscopy (HAADF-STEM) with spherical aberration correction were made with a FEI Talos F200x transmission electron microscope operated at 300 kV.

X-ray photoelectron spectroscopy (XPS) characterizations were carried out by using a ThermoFischer, ESCALAB Xi+ electron spectrometer. The vacuum degree of the analysis chamber was 8 × 10^{-10} Pa. The X-ray source is a monochromatic Al Kα source (Mono Al Kα) with an energy of 1486.6 eV. X-ray source with emission of 16 mA and anode HT of 12.5 KV.

Powder X-ray diffraction (XRD) was conducted using a Bruker D8 ADVANCE X-ray diffractometer.

The Inductively Coupled Plasma Optical Emission Spectrum (ICP) was carried out by a PE Avio 200 spectrometer.

Raman spectra were recorded by a Labram HR 122 Evolution confocal laser Raman instrument with a 532 nm laser excitation source.

X-ray absorption fine structure (XAFS) spectra data were collected at beamline 7-BM of the National Synchrotron Light Source II at Brookhaven National Laboratory, NY. XAFS data was implemented on Athena and Artemiss software[1]. WT-EXAFS data was calculated on Hama Fortran[2, 3]. For Wavelet Transform analysis, the χ(k) exported from Athena was imported into the Hama Fortran code. The parameters were listed as follow: R range, 0 - 6 Å, k range, 0 – 12 $Å^{-1}$ for samples; k weight, 3; and Morlet function with κ=10, σ=1 was used as the mother wavelet to provide the overall distribution.

Electrode preparation and electrochemical measurements

The self-supporting catalysts like LDH*/NFO and LDH*/NFO were cut to 1 × 1 cm^2, acting as the working electrode directly. The electrode area was uniformly normalized to 2.4 cm^2. For power catalysts (RuO_2 and FC), the catalyst ink was prepared first. Typically, 5 mg of the catalyst power was dispersed into 1 mL of the solution containing 0.9 mL of ethanol, 50 μL of deionized water and 0.05 mL of Nafion solution (5 wt%). The mixture was sonicated for 30 min to form a homogeneous catalyst ink solution. Subsequently, 205 μL of the ink was taken out and carefully dropped onto a piece of pre-cleaned NF (1 × 1 cm^2) under vacuum. Finally, a working electrode with a catalyst loading of 0.512 mg/cm^2 was obtained. The electrochemical measurements were performed in a three-electrode system with an electrochemical analyzer (CS310H). Briefly, the prepared NF electrode as the working electrode, Ag/AgCl (saturated KCl) and graphite rod as the reference electrode and counter electrode, respectively. The potentials measured through Ag/AgCl were converted into the reversible hydrogen electrode (RHE) using the following equation:

$$E_{RHE} = E_{Ag/AgCl} + 0.198 + 0.059 \times pH.$$

Before the OER test, N_2 was introduced for 30 min to remove the dissolved gas and supplied it throughout the test. Cyclic voltammetry (CV) was performed at first to activate and stabilize the working electrode with a scanning rate of 100 mV/s. Linear sweep voltammetry (LSV) was performed at a slow rate of 1 mV/s for the OER activity estimate and 2 mV/s for the HER and full water splitting test. To research the behavior of electrodes, electrochemical impedance spectra (EIS) were tested at the overpotential of 1.5 V (vs. RHE) and 0.1 V (vs. RHE) for OER and HER from 10^5 Hz to 10^{-2} Hz, respectively.

Calculation of the TOF

The turnover frequency (TOF) was derived to expose the real activity of the catalyst by the following equation[4]

$$\mathrm{TOF} = \frac{2|j|A}{mFn}$$

In which j is the current density, A is the area of the electrode, m is the number of transfer electrons to form O_2 (4 electrons for OER), and n is the number of active sites. The value of n of catalysts was estimated from the CV data collected from -0.2 V to 0.6 V (vs. RHE) in a buffer solution (Na_2HPO_4 and NaH_2PO_4, pH=7) according to the following equation:

$$n = \frac{Q}{2F}$$

where F is the Faradic constant (96485 C/mol), and Q is the quantity of electricity of CV cures.

Calculation of the Faradic enfficence

To analyze the Faradaic efficiency (FE) of LDH*/NFO, an H-type electrolysis cell with an anion exchange membrane() was assembled. Before the test, the anion exchange membrane was treated sequentially with 5% H_2SO_4, KOH and deionized water at 80°C. Chronopotentiometry polarization was employed for electrolysis at 100 mA. Anode and cathode gases were collected using the drainage method. The Faradaic efficiency was calculated by the following equation:

$$\mathrm{FE} = 4\frac{n_{\mathrm{O}_2}F}{Q}$$

F is the Faradic constant, *Q* is the quantity of applied electricity, n_{O_2} is the amount of O_2.

$$n_{\mathrm{O}_2} = \frac{V}{V_m}$$

Where V_m is 24.05 L mol^{-1} at 20 ℃ and 100 kPa.

Theoretical calculations

Density functional theory (DFT) calculations use the Vienna ab-initio simulation package (VASP) program to optimize the geometry structure and determine the binding energy (ΔE) between FeCo-LDH (defined as E_{LDH}) and $Ni(OH)_2$ (or Ni, defined as E_{sub}). The binding energy (ΔE) was calculated by the equation: $\Delta E = E_{sub+LDH} - E_{LDH} - E_{sub}$, where $E_{sub+LDH}$ is the energy of LDH-$Ni(OH)_2$ (or Ni). The Perdew-Burke-Ernzerhof (PBE) exchange-correlation function in the generalized gradient approximation (GGA) method was used to set the cut-off energy as 400 eV. The energy and force convergence criteria are 10^{-5} eV and 0.02 eV/Å. The Hubbard-U correction (DFT + U) used to enhance the description of metal *d* orbital electrons in the FeCo-LDH and $Ni(OH)_2$. We selected the previously reported U values of 6.2 eV, 2.56 eV and 3.5 eV for Ni, Fe and Co atoms, respectively. The vacuum spacing was set as 15 Å for all periodic slab calculations. A 2 × 2 × 1 Monkhorst-pack k-point was selected. The lattice oxidation mechanism (LOM) of OER in alkaline was enabled for the analysis of the Gibbs energy barrier.

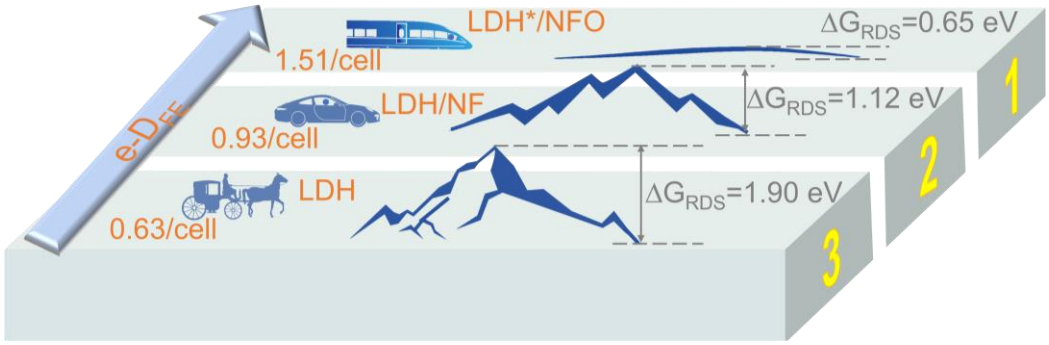

Figure S1. The schematic diagram of e-D_{FE} for OER.

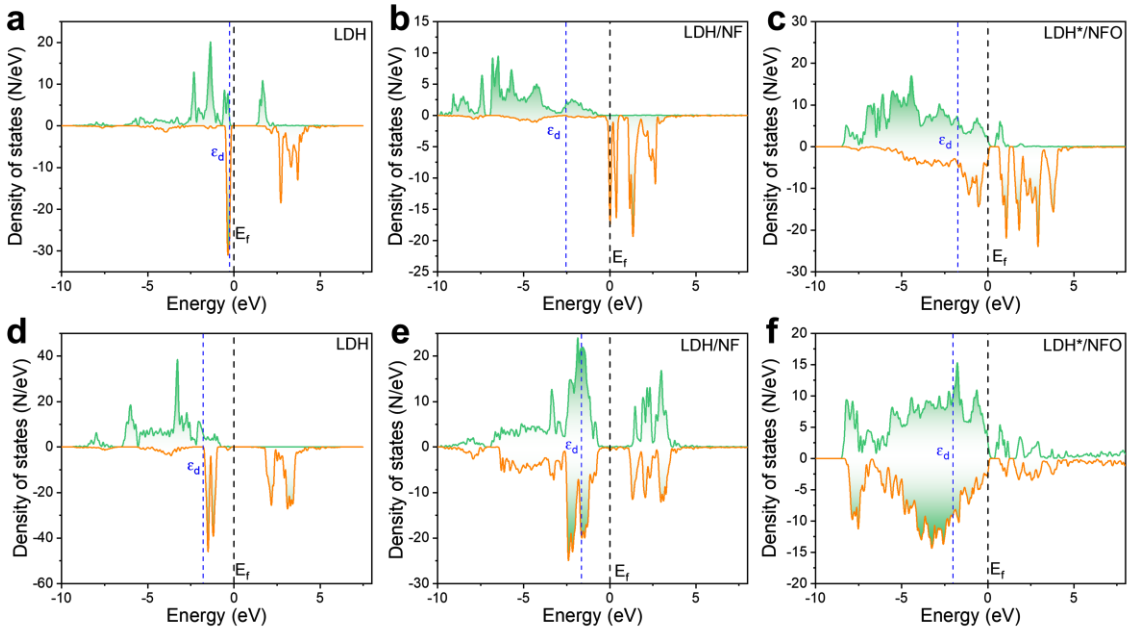

Figure S2. (a-c) The DOS of Fe for LDH, LDH/NF and LDH*/NFO. (d-f) The DOS of Co for LDH, LDH/NF and LDH*/NFO.

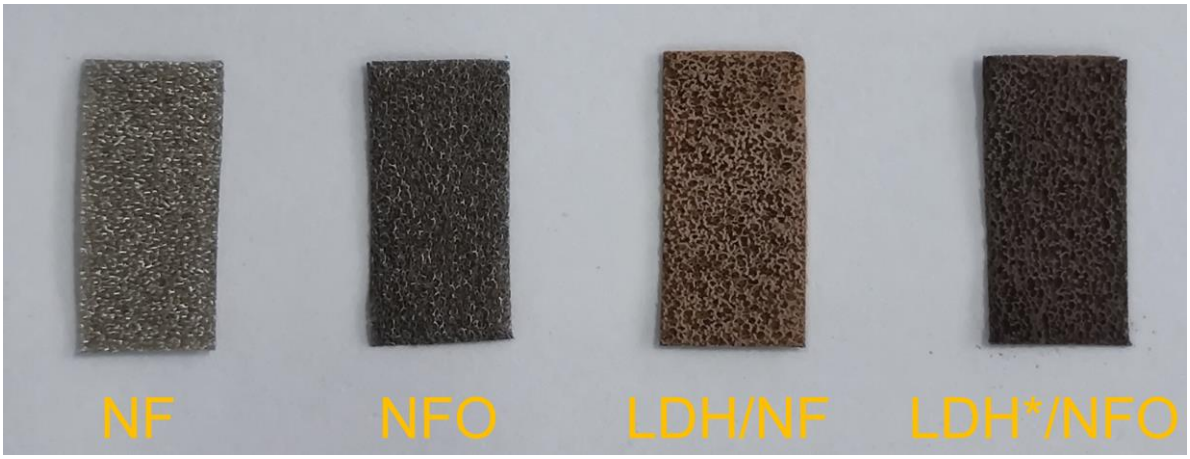

Figure S3. The optical photos of the prepared catalysts.

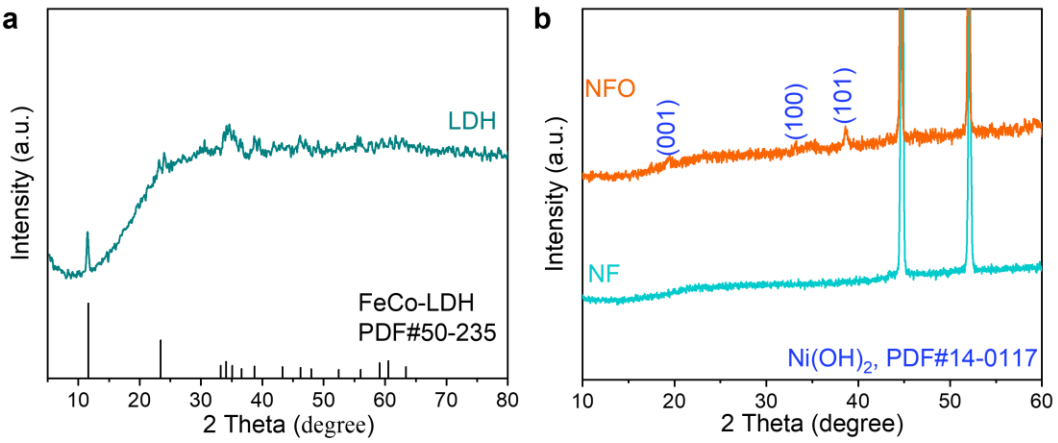

Figure S4. XRD pattern of (a) LDH and (b) NFO.

Table S1. The lattice constant of the optimized configurations of LDH, LDH/NF and LDH/NFO.

Lattice constant	LDH	LDH/NF	LDH*/NFO
a	3.120 Å	3.041 Å	3.126 Å
b	3.120 Å	3.042 Å	3.127 Å

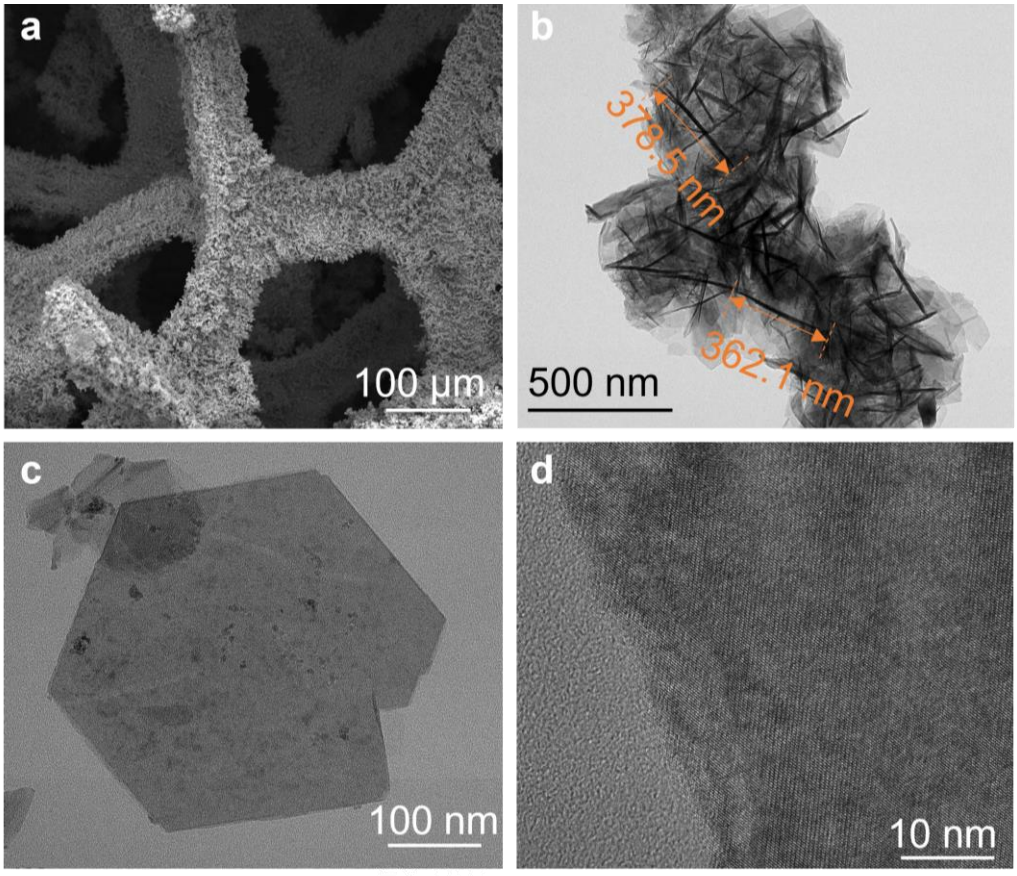

Figure S5. SEM mage (a) and TEM images (b-d) of LDH*/NF.

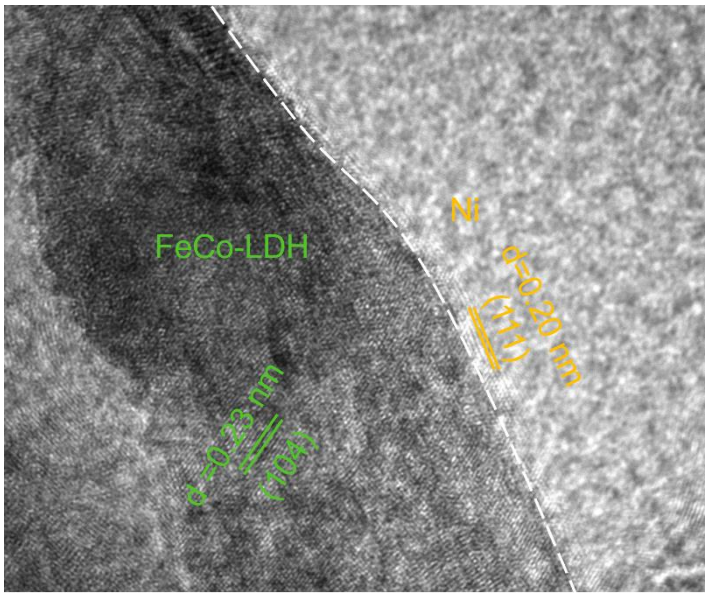

Figure S6. The HRTEM image of LDH/NF.

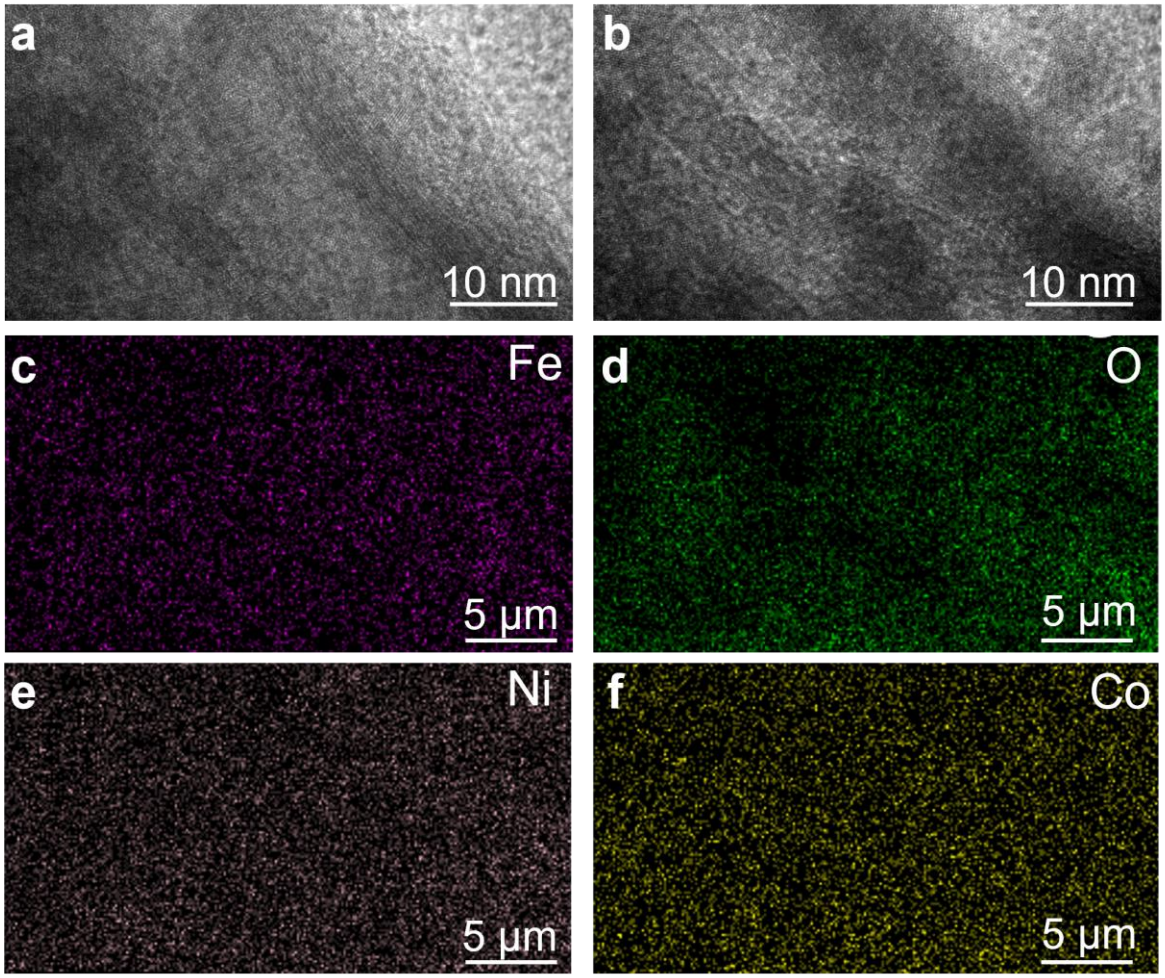

Figure S7. (a-b) The TEM image and (c-f) EDX-mapping images of LDH/NF.

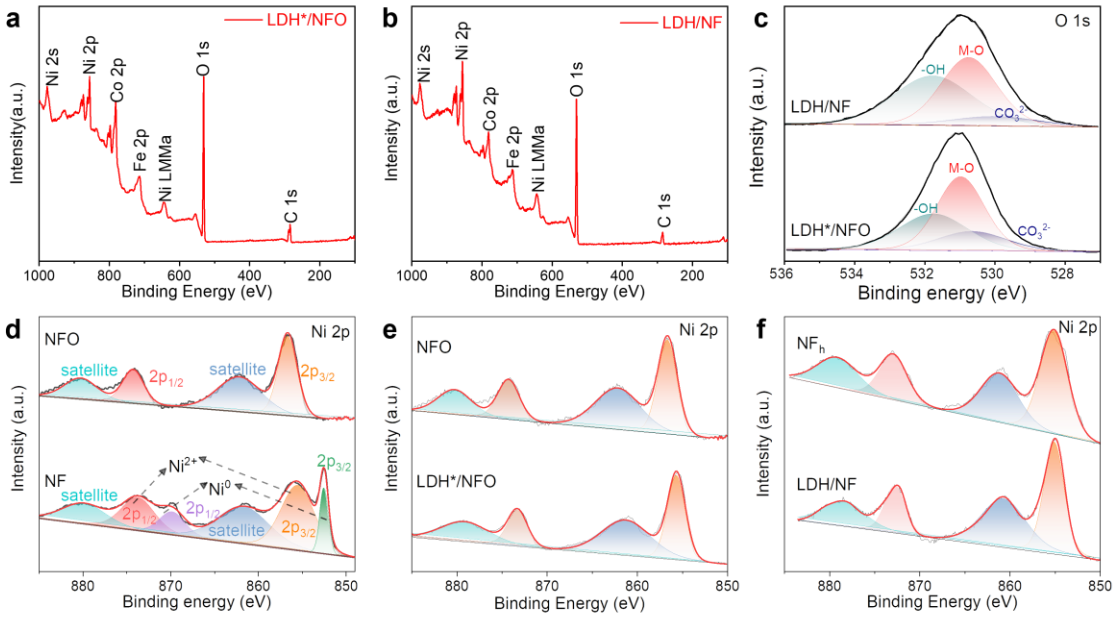

Figure S8. XPS spectra of (a) LDH*/NFO and (b) LDH/NF. (c) High-resolution XPS spectra of O 1s for LDH/NF and LDH*/NFO. (d-f) High-resolution XPS spectra of Ni 2p for various catalyst.

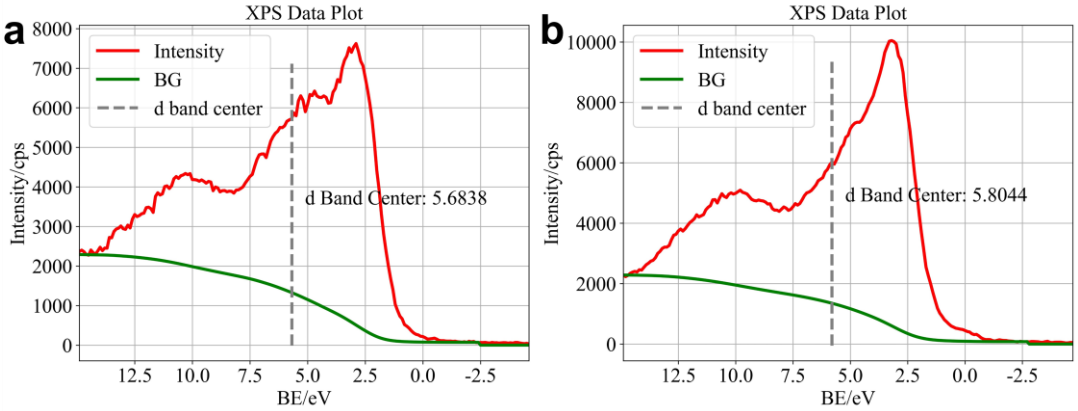

Figure S9. VBS of (a) LDH and (b) LDH*/NFO. The d-band center of the VBS is given by the following equation: $\frac{\int R_\varepsilon \varepsilon d\varepsilon}{\int R_\varepsilon d\varepsilon}$. R_ε is the intensity of VBS after background subtraction.

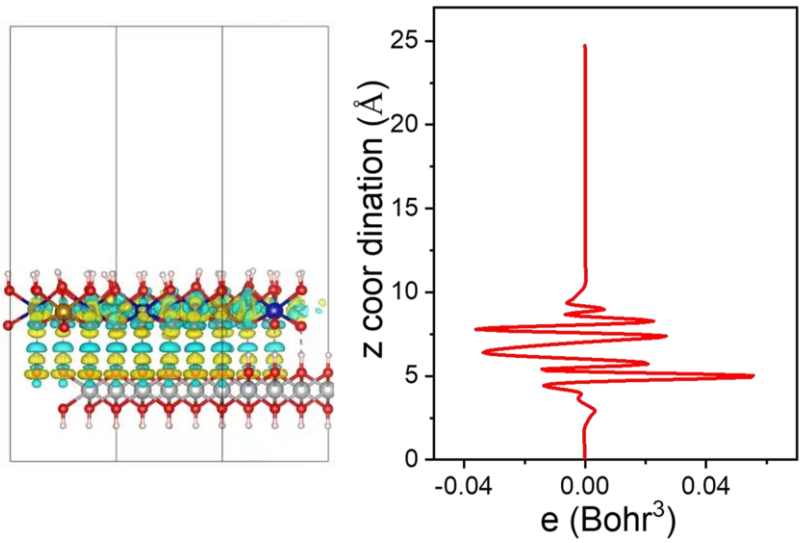

Figure S10. Charge density differential diagram of LDH*/NFO.

Table S2. Bader charge analysis of Fe and Co for LDH, LDH/NF and LDH*/NFO.

Element	LDH	LDH/NF	LDH*/NFO
Fe	6.62	6.41	6.30
Co	7.69	7.73	7.56

Table S3. The comparison of overpotential (η_{10} and η_{100}) and Tafel slope for LDH*/NFO with recently reported LDH-based catalysts.

Catalyst	η_{10} (mV)	η_{100} (mV)	Tafel (mV dec^{-1})	Reference
LDH*/NFO	**216**	**246**	**38.24**	**This work**
	214 $_{iR}$	**237$_{iR}$**		
h-$Co_{0.34}Fe_{0.33}Ni_{0.33}$-LDH	195	235	53	[5]
FeNiLDH	202	270	55.7	[6]
F-CoFeLDH	230	349	41	[7]
NiFe-LDH-Bir	258	315	43	[8]
CeO_{2-x}/NiFe-LDH	216	300	74.1	[9]
Co-LDH@MOF	187	286	59	[10]
NiFeLDH/GQD	189	273	23.6	[11]
NiFeW-LSH/NF	-	247	55	[12]
NiFeLDH-PANI	220	270	44	[13]
Co-NiFeLDH	230	335	44	[14]
FeNiLDH-V_2C	250	306	46.5	[15]
NiFe-LDHDSNCs	230	295	71	[16]
NiFeVLDH/KB	181	395	47	[17]
CoFeLDH/GF	252	285	52	[18]
W-FeCoLDH	205	330	56	[19]

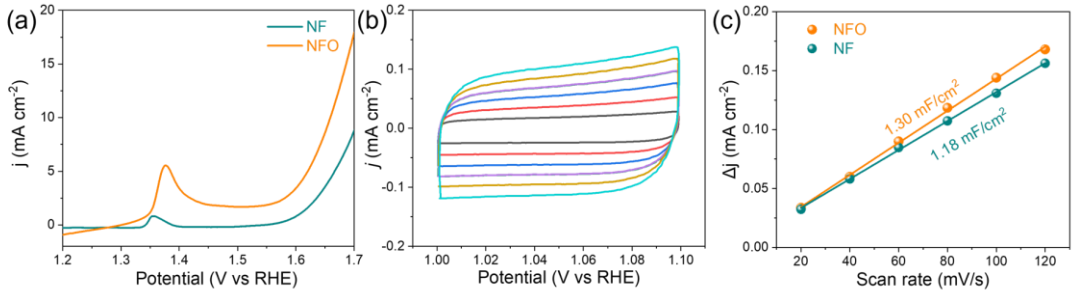

Figure S11. (a) LSV curves of NFO and NF. (b) CV curves of NFO. (c) The C_{dl} of NFO and NF.

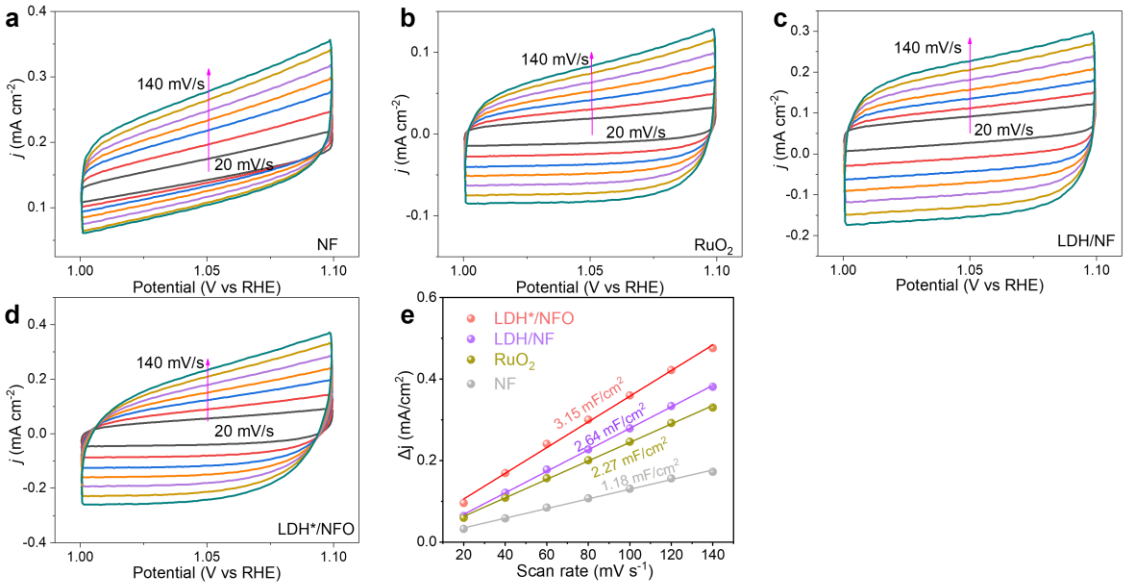

Figure S12. The CV curves of (a) NF, (b) RuO_2, (c) LDH/NF and (d) LDH*/NFO at the potential range of 1.0 V ~ 1.1 V. (e) The C_{dl} of RuO_2, NF, LDH/NF and LDH*/NFO.

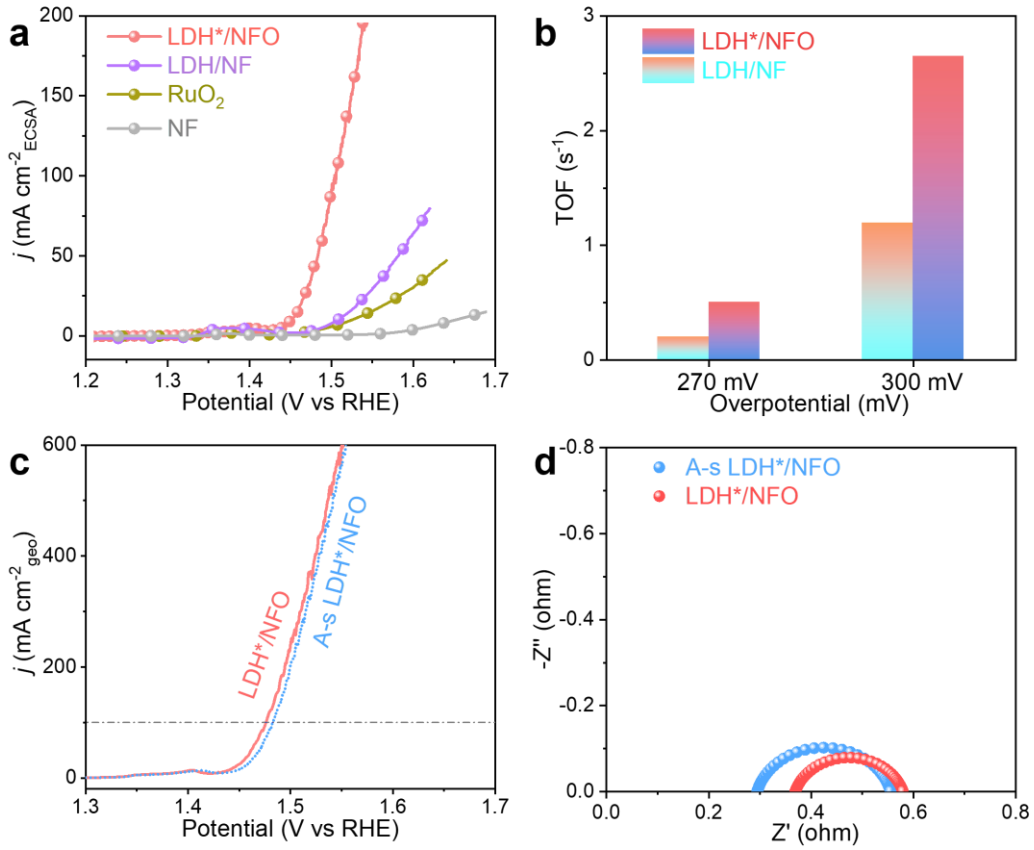

Figure S13. (a) ECSA-normalized polarization curves of NF, LDH/NF, LDH*/NFO and RuO_2. (b) TOF values of LDH/NF and LDH*/NFO at the overpotential of 270 mV and 300 mV. (c) Geometry-normalized polarization curves and (d) Nyquist plots at 1.53 V (vs RHE) of LDH*/NFO before and after the stability test.

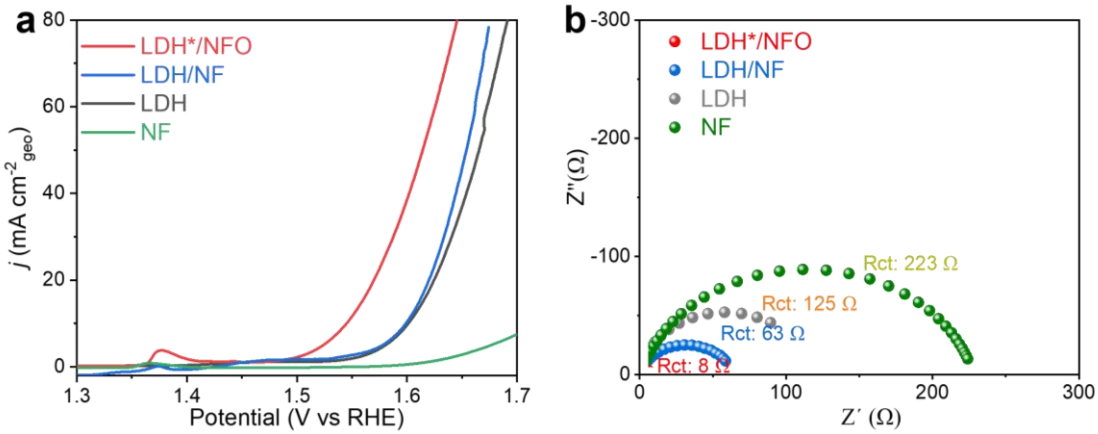

Figure S14. (a) Geometry-normalized polarization curves and (b) Nyquist plots at 1.53 V of LDH, LDH/NF (power) and LDH*/NFO (power) with a loading of 0.2 mg cm^{-2}.

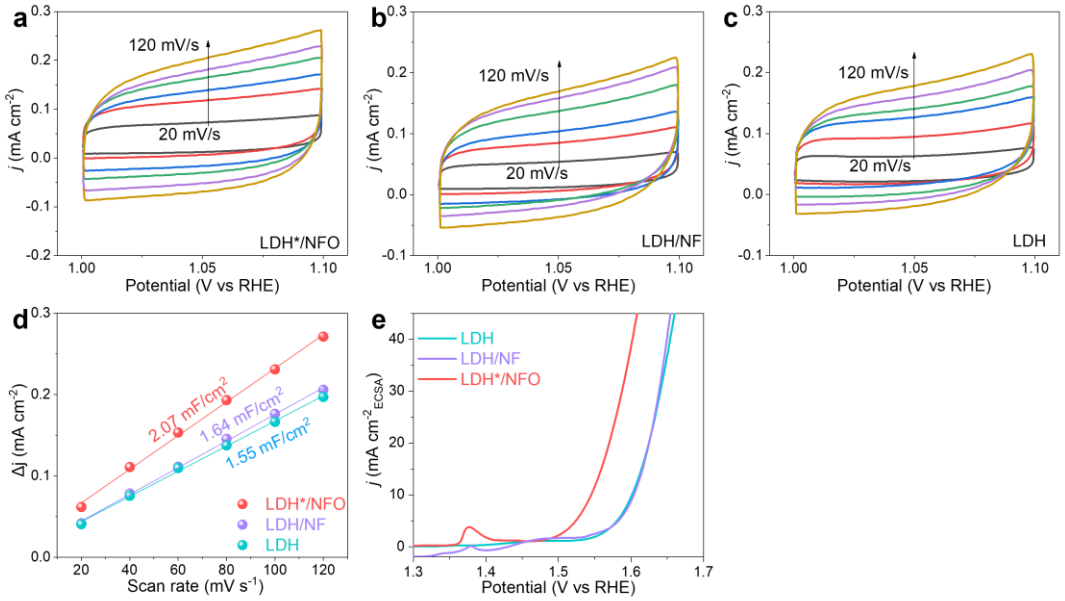

Figure S15. (a) LDH*/NFO (power), (b) LDH/NF (power), (c) LDH. (d) C_{dl} and (e) ECSA-normalized polarization curves of LDH, LDH/NF (power) and LDH*/NFO (power).

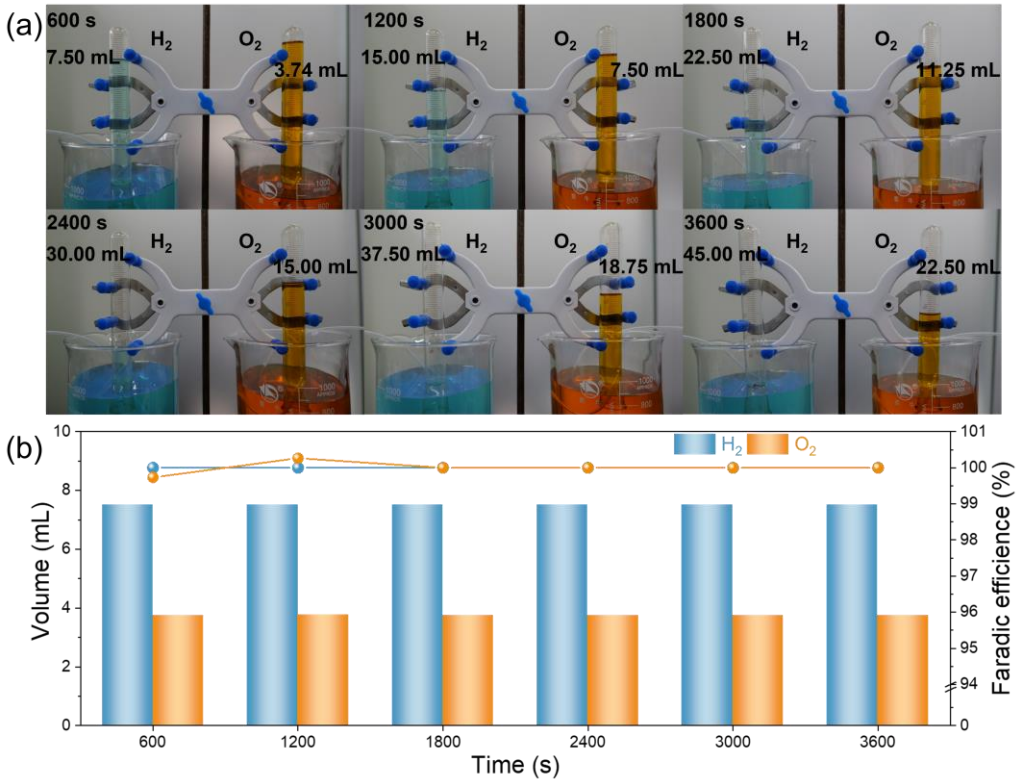

Figure S16. (a) The optical photos of the FE test at 100 mA. (b) The gas volume and FE of anode and cathode.

Table S4. The comparison of stability for LDH*/NFO with recently reported OER catalysts.

Catalyst	Stability$_{100\ mA/cm2}$ (h)	Reference
LDH*/NFO	**3500**	**This work**
FeCoNi-PBA	75	[20]

$Fe_xNi_{2-x}P_4O_{12}$/RGO	100	[21]
WO_2-$NaWO_3$@FeOOH/NF	120	[22]
$NiCo_2O_4$@FeO_x	300	[23]
NiCo-LDH/NiCoPi	200	[24]
$(CrMnFeCoNi)S_x$	10	[25]
$Co_{3-x}Fe_xMo_3N$	90	[26]
NiSi	200	[27]
Ni-NM@G-10	50	[28]
$NiO_x(OH)_y$	1000	[29]
Ni-O-G SACs	50	[30]
P-$Ni_{0.75}Fe_{0.25}Se_2$	120	[31]
FeNiCoCrMn-G HEG	36	[32]
Ni-BDC-1R	100	[33]
Fe_3O_4/FeS_2	36	[34]
FeCoPd NPs	100	[35]
NiFeLDH@PANi-CF	100	[36]
B,N-GQDs/MOF-d-LDH	24	[37]
NLOS-X@CC	72	[38]

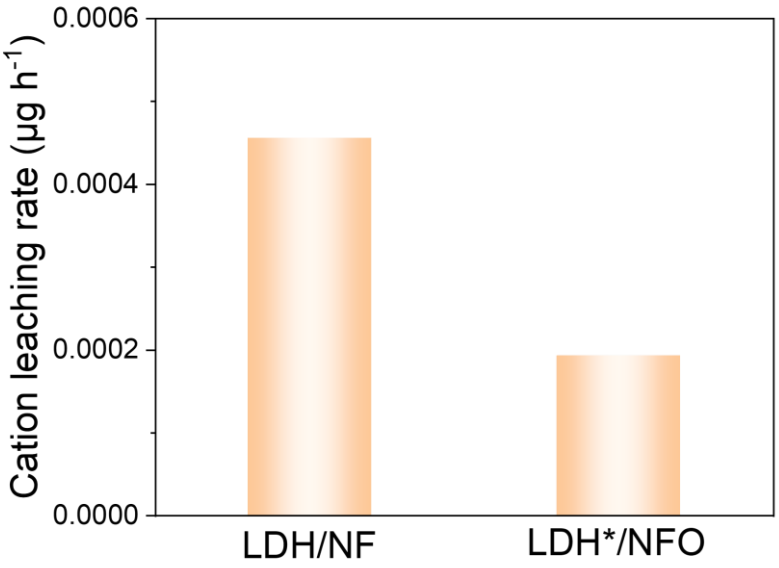

Figure S17. Ni leaching rate of LDH/NF and LDH*/NFO during stability test.

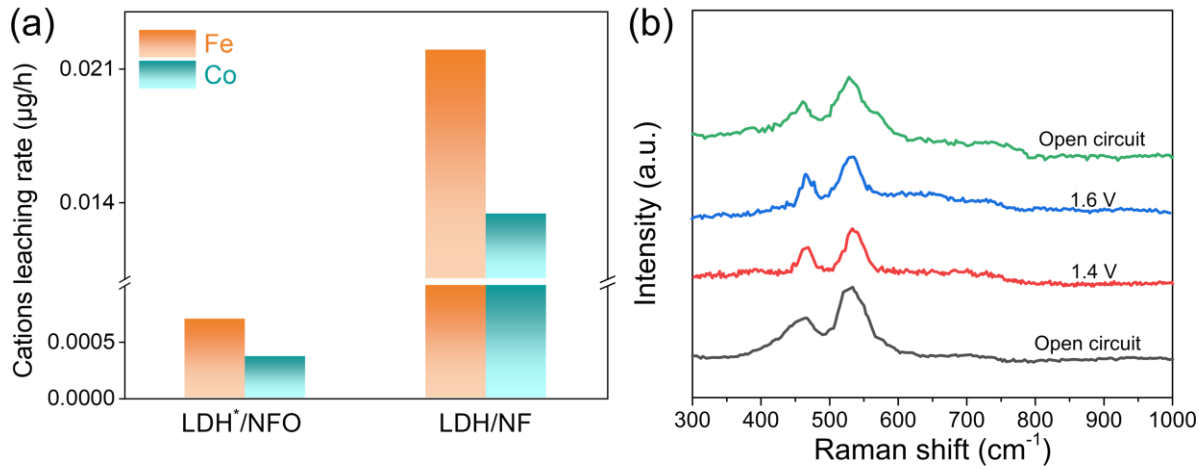

Figure S18. Cations leaching rate of LDH/NF and LDH*/NFO. In-suit Raman spectra of LDH*/NFO.

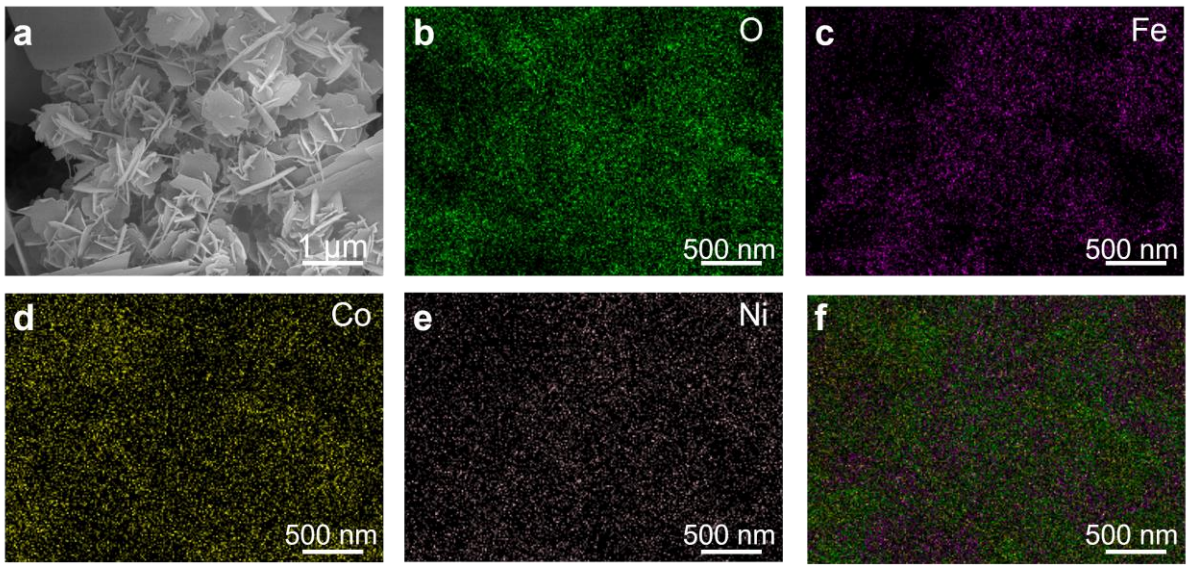

Figure S19. EDS analysis of A-LDH*/NFO.

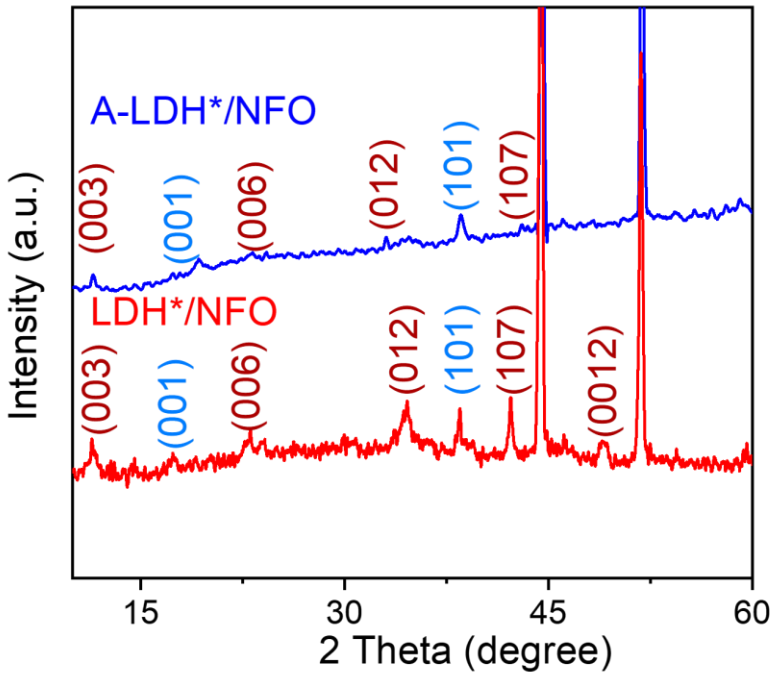

Figure S20. XRD pattern of LDH*/NFO and A-LDH*/NFO.

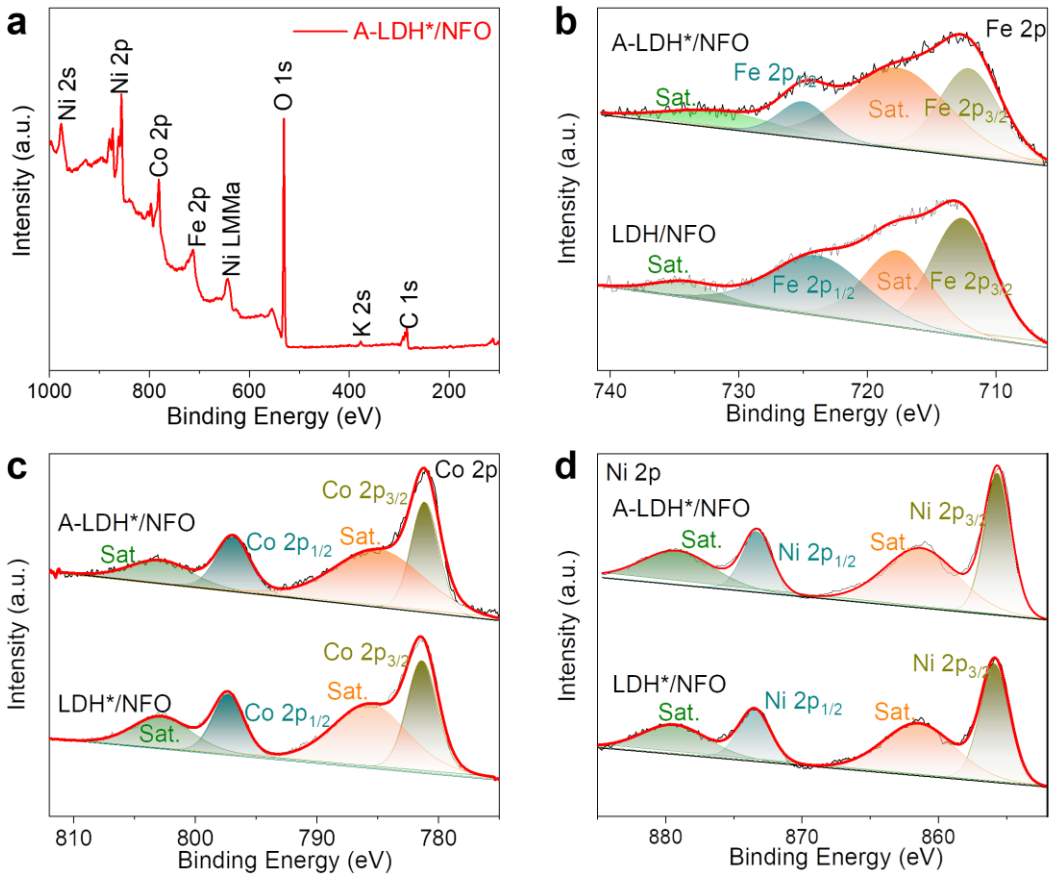

Figure S21. (a) XPS spectra, (b) high-resolution XPS spectra of Fe 2p, (c) Co 2p and (d) Ni 2p of LDH*/NFO and A-LDH*/NFO.

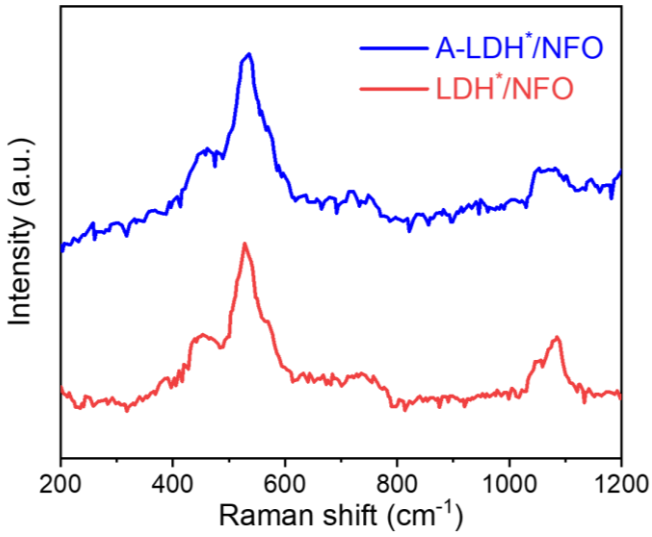

Figure S22. Raman spectra of LDH*/NFO and A-LDH*/NFO.

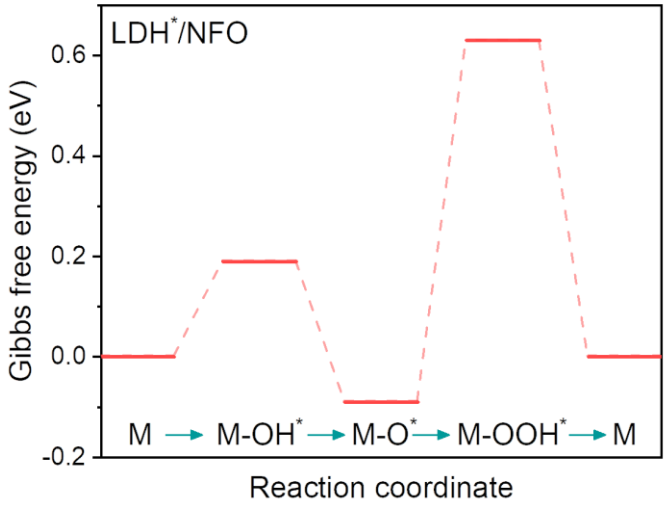

Figure S23. The four-electron associative process of AEM and Gibbs free energy diagrams of LDH*/NFO.

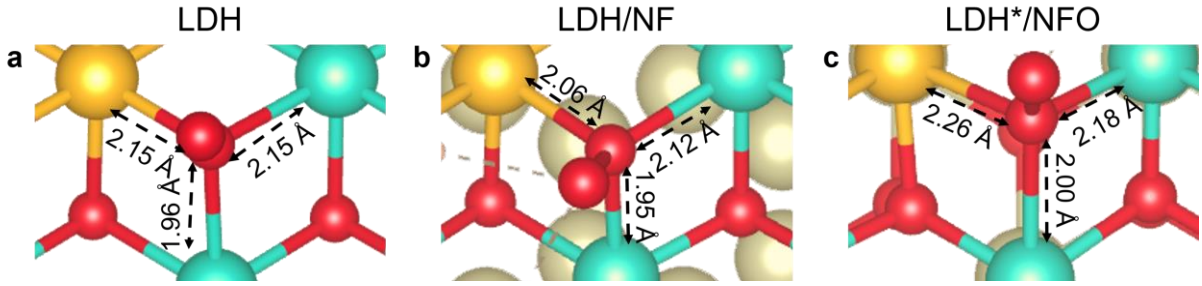

Figure S24. The crystal structure at the step of O_2 desorption. a LDH, b LDH/NF and c LDH*/NFO.

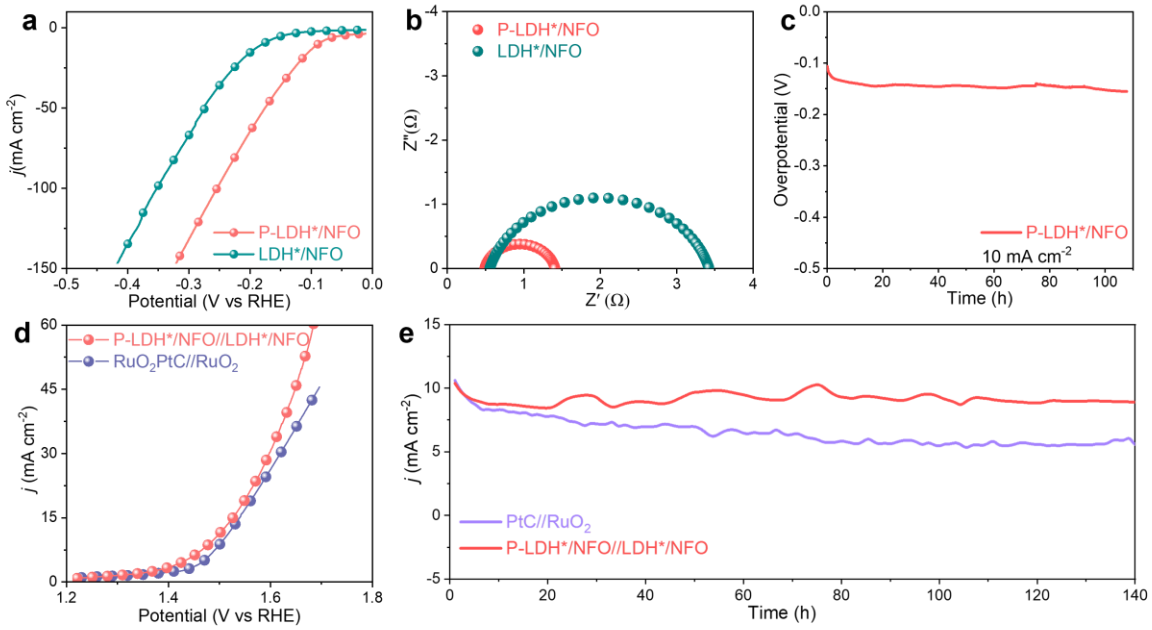

Figure S25. (a) LSV curves of LDH*/NFO and P-LDH*/NFO with a scan rate of 2 mV s^{-1}. (b) The Nyquist plots of LDH*/NFO and P-LDH*/NFO at -0.1 V (vs RHE). (c) Stability testing of P-LDH*/NFO at the current density of 10 mA cm^{-2}. (d) The two-electrolyte water splitting activity of P-LDH*/NFO//LDH*/NFO and PtC//RuO_2 with a scan rate of 2 mV s^{-1}. (e) Chronoamperometry curves of P-LDH*/NFO//LDH*/NFO and PtC//RuO_2 at a potential for the current density of 10 mA cm^{-2}.

References

1 B. Ravel and M. Newville, *J. Synchrotron Radiat.*, 2005, **12**, 537-541.

2 H. Funke, A.-C. Scheinost and M. Chukalina, *Phys. Rev. B*, 2005, **71**, 094110.

3 H. Funke, M. Chukalina and A.-C. Scheinost, *J. Synchrotron Radiat.*, 2007, **14**, 426-432.

4 W. Huang, J. Li, X. Liao, R. Lu, C. Ling, X. Liu, J. Meng, L. Qu, M. Lin, X. Hong, X. Zhou, S. Liu, Y. Zhao, L. Zhou and L. Mai, *Adv. Mater.*, 2022, **34**, e2200270.

5 H. Sun, L. Chen, Y. Lian, W. Yang, L. Lin, Y. Chen, J. Xu, D. Wang, X. Yang, M.-H. Rummerli, J. Guo, J. Zhong, Z. Deng, Y. Jiao, Y. Peng and S. Qiao, *Adv. Mater.*, 2020, **32**, e2006784.

6 J. He, X. Zhou, P. Xu and J. Sun, *Nano Energy*, 2021, **80**, 100540.

7 M. Li, Y. Gu, Y. Chang, X. Gu, J. Tian, X. Wu and L. Feng, *Chem. Eng. J.*, 2021, **425**, 130686.

8 Z. Chen, M. Ju, M. Sun, L. Jin, R. Cai, Z. Wang, L. Dong, L. Peng, X. Long, B. Huang and S. Yang, *Angew. Chem. Int. Ed.*, 2021, **60**, 9699-9705.

9 Y. Du, D. Liu, T. Li, Y. Yan, Y. Liang, S. Yan and Z. Zou, *Appl. Catal. B*, 2022, **306**, 121146.

10 Z. Li, X. Zhang, Y. Kang, C.-C. Yu, Y. Wen, M. Hu, D. Meng, W. Song and Y. Yang, *Adv. Sci.*, 2021, **8**, 2002631.

11 X. Guo, X. Zheng, X. Hu, Q. Zhao, L. Li, P. Yu, C. Jing, Y. Zhang, G. Huang, B. Jiang, C. Xu and F. Pan, *Nano Energy*, 2021, **84**, 105932.

12 L. Wu, L. Yu, F. Zhang, D. Wang, D. Luo, S. Song, C. Yuan, A. Karim, S. Chen and Z. Ren, *J. Mater. Chem. A*, 2020, **8**, 8096-8103.

13 J. Zhang, H. Zhang and Y. Huang, *Appl. Catal. B*, 2021, **297**, 120453.

14 Y. Yang, S. Wei, Y. Li, D. Guo, H. Liu and L. Liu, *Appl. Catal. B*, 2022, **314**, 121491

15 Y. Chen, H. Yao, F. Kong, H. Tian, G. Meng, S. Wang, X. Mao, X. Cui, X. Hou and J. Shi, *Appl. Catal. B*, 2021, **297**, 120474.

16 J. Zhang, L. Yu, Y. Chen, X. F. Lu, S. Gao and X.-W.-D. Lou, *Adv. Mater.*, 2020, **32**, e1906432.

17 B. Zhang, Z. Wu, W. Shao, Y. Gao, W. Wang, T. Ma, L. Ma, S. Li, C. Cheng and C. Zhao, *Angew. Chem. Int. Ed.*, 2022, **61**, e202115331.

18 B. Deng, J. Liang, L. Yue, T. Li, Q. Liu, Y. Liu, S. Gao, A.-A. Alshehri, K.-A. Alzahrani, Y. Luo and X. Sun, *Chin. Chem. Lett.*, 2022, **33**, 890-892.

19 X. Liang, F.-K. Chiang, L. Zheng, H. Xiao, T. Zhang, F. Zhang and Q. Gao, *Chem. Commun.*, 2022, **58**, 7678-7681.

20 T.-X. Nguyen, K.-H. Yang, Y.-J. Huang, Y.-H. Su, O. Clemens, R.-K. Xie, Y.-J. Lin, J.-F. Lee and J.-M. Ting, *Chem. Eng. J.*, 2023, **474**, 145831.

21 L. Lin, Y. Wang, Q. Ye, Y. Zhao and Y. Cheng, *Appl. Catal. B*, 2023, **334**, 122834.

22 J. Liu, G. Qian, H. Zhang, J. Chen, Y. Wang, H. He, L. Luo and S. Yin, *Chem. Eng. J.*, 2021, **426**, 131253.

23 C. Wei, N. Heng, Z. Wang, X. Song, Z. Sun, X. Zhu, J. He, Y. Zhao and X. Wang, *Chem. Eng. J.*, 2022, **435**, 134672.

24 S. Zhou, Y. Liu, J. Li, Z. Liu, J. Shi, L. Fan and W. Cai, *Green Energy Environ.*, 2022, **12**, 003.

25 M. Cui, C. Yang, B. Li, Q. Dong, M. Wu, S. Hwang, H. Xie, X. Wang, G. Wang and L. Hu, *Adv. Energy Mater.*, 2020, **11**, 2002887.

26 C. Zhong, J. Zhang, L. Zhang, Y. Tu, H. Song, L. Du and Z. Cui, *ACS Energy Lett.*, 2023, **8**, 1455-1462.

27 I. Mondal, J.-N. Hausmann, G. Vijaykumar, S. Mebs, H. Dau, M. Driess and P.-W. Menezes, *Adv. Energy Mater.*, 2022, **12**, 2200269.

28 J. Zhang, W.-J. Jiang, S. Niu, H. Zhang, J. Liu, H. Li, G.-F. Huang, L. Jiang, W.-Q. Huang, J.-S. Hu and W. Hu, *Adv. Mater.*, 2020, **32**, e1906015.

29 D. Liu, Y. Yan, H. Li, D. Liu, Y. Yang, T. Li, Y. Du, S. Yan, T. Yu, W. Zhou, P. Cui and Z. Zou, *Adv. Mater.*, 2022, **35**, e2203420.

30 Y. Li, Z.-S. Wu, P. Lu, X. Wang, W. Liu, Z. Liu, J. Ma, W. Ren, Z. Jiang and X. Bao, *Adv. Sci.*, 2020, **7**, e1903089.

31 Y. Huang, L.-W. Jiang, B.-Y. Shi, K.-M. Ryan and J.-J. Wang, *Adv. Sci.*, 2021, **8**, e2101775.

32 T.-X. Nguyen, Y.-H. Su, C.-C. Lin, J. Ruan and J.-M. Ting, *Adv. Sci.*, 2021, **8**, e2002446.

33 L. Zhang, J. Wang, K. Jiang, Z. Xiao, Y. Gao, S. Lin and B. Chen, *Angew. Chem. Int. Ed.*, 2022, **61**, 2214794.

34 M.-J. Wang, X. Zheng, L. Song, X. Feng, Q. Liao, J. Li, L. Li and Z. Wei, *J. Mater. Chem. A*, 2020, **8**, 14145-14151.

35 A. Kumar, S.-K. Purkayastha, A.-K. Guha, M.-R. Das and S. Deka, *J. Mater. Chem. A*, 2022, **10**, 23731-23743.

36 N. Lingappan, I. Jeon and W. Lee, *J. Mater. Chem. A*, 2023, **11**, 17797-17809.

37 M. Rinawati, Y.-X. Wang, W.-H. Huang, Y.-T. Wu, Y.-S. Cheng, D. Kurniawan, S.-C. Haw, W.-H. Chiang, W.-N. Su and M.-H. Yeh, *Carbon*, 2022, **200**, 437-447.

38 K. Yu, H. Yang, H. Zhang, H. Huang, Z. Wang, Z. Kang, Y. Liu, P.-W. Menezes and Z. Chen, *Nano-Micro Lett.*, 2023, **15**, 186.